OUKA
The University of Osaka
Institutional Knowledge Archive

Title	Enhanced work hardening in ferrite and austenite of duplex stainless steel at 200 K: In situ neutron diffraction study
Author(s)	Yamashita, Takayuki; Koga, Norimitsu; Wenqi, Mao et al.
Citation	Materials Science and Engineering: A. 2025, 941, p. 148602
Version Type	VoR
URL	https://hdl.handle.net/11094/102608
rights	This article is licensed under a Creative Commons Attribution-NonCommercial-NoDerivatives 4.0 International License.
Note	

The University of Osaka Institutional Knowledge Archive : OUKA

https://ir.library.osaka-u.ac.jp/

The University of Osaka

Materials Science & Engineering A 941 (2025) 148602

Contents lists available at ScienceDirect

Materials Science & Engineering A

journal homepage: www.elsevier.com/locate/msea

Enhanced work hardening in ferrite and austenite of duplex stainless steel at 200 K: *In situ* neutron diffraction study

Takayuki Yamashita [a,*], Norimitsu Koga [b], Mao Wenqi [c], Wu Gong [d], Takuro Kawasaki [d], Stefanus Harjo [d,**], Hidetoshi Fujii [a], Osamu Umezawa [e]

[a] Joining and Welding Research Institute, Osaka University, 11-1 Mihogaoka, Ibaraki, Osaka, 567-0047, Japan
[b] Faculty of Mechanical Engineering, Institute of Science and Engineering, Kanazawa University, Kakuma-machi, Kanazawa, Ishikawa, 920-1192, Japan
[c] Key Laboratory of Electromagnetic Processing of Materials (Ministry of Education) Northeastern University, Shenyang, 110819, China
[d] J-PARC Center, Japan Atomic Energy Agency, 2-4 Shirakata, Tokai, Naka, Ibaraki, 319-1195, Japan
[e] Faculty of Engineering, Yokohama National University, 79-5 Tokiwadai, Hodogaya, Yokohama, 240-8501, Japan

ARTICLE INFO

Keywords:
Duplex stainless steel
Neutron diffraction
Stress partitioning
Stacking fault
Low temperature

ABSTRACT

Ferrite-austenite duplex stainless steels exhibit excellent strength and ductility, making them attractive for applications in extreme environments. In this study, *in situ* neutron diffraction measurements were conducted during tensile testing at 293 K and 200 K to investigate stress partitioning and phase-specific deformation behavior at low temperatures. Phase stress was derived using a texture-compensated method to accurately evaluate stress partitioning and each phase's contribution to the overall strength. Regardless of temperature, ferrite exhibited higher phase stress than austenite, acting as the harder phase. At 200 K, both ferrite and austenite showed increased strength and work hardening, with austenite exhibiting significant stacking fault development in addition to dislocation migration. The plastic deformation mode of ferrite at 200 K was similar to that at 293 K, governed by dislocation migration, but it became more effective. The stress contributions of ferrite and austenite during plastic deformation were comparable at both temperatures. No martensitic transformation was observed in the tested temperature range. The combination of strengthening and enhanced work hardening in both phases contributed to the high strength of duplex stainless steel at 200 K while maintaining ductility comparable to that at 293 K.

1. Introduction

Dual-phase steels and alloys, which consist of two phases with different crystal structures and mechanical properties, combine the characteristics of both phases and exhibit superior properties that are difficult to achieve in single-phase materials [1–3]. Among these, duplex stainless steel (DSS) [4], composed of ferrite (α) with a body-centered cubic (BCC) structure and austenite (γ) with a face-centered cubic (FCC) structure, is one of the most representative dual-phase alloys. It exhibits high strength, superior ductility, and excellent corrosion resistance. Stress partitioning between the phases with different strength and deformability is considered a key factor in achieving the outstanding mechanical properties of DSS [5,6]. To clarify stress partitioning behavior in DSS, various methods have been employed, including nanoindentation [7,8], digital image correlation [9], and *in situ* diffraction techniques using synchrotron X-rays [10–12] and neutron beams [13–16]. In particular, *in situ* neutron and X-ray diffraction analyses provide critical insights not only into stress partitioning but also into phase-specific deformation behavior, phase fraction evolution, texture development, and dislocation dynamics. Consequently, these measurements have been widely applied not only to DSSs but also to various steels with complex microstructures [17–19]. Tsuchida et al. [10] conducted *in situ* neutron diffraction measurements during deformation on two types of DSS with different mechanical properties to evaluate stress partitioning between α and γ phases (phase stresses) and among grains (intergranular stresses). They found that intergranular stress partitioning in the γ phase was greater than that in the α phase and highlighted that phase stress partitioning, the work hardening of γ, and the phase fraction of γ are key factors influencing the work hardening behavior of DSS. Matsushita et al. [16] performed *in situ* neutron

* Corresponding author.
** Corresponding author.
E-mail addresses: yamashita.takayuki.jwri@osaka-u.ac.jp (T. Yamashita), stefanus.harjo@j-parc.jp (S. Harjo).

https://doi.org/10.1016/j.msea.2025.148602
Received 6 March 2025; Received in revised form 25 April 2025; Accepted 29 May 2025
Available online 30 May 2025
0921-5093/© 2025 The Authors. Published by Elsevier B.V. This is an open access article under the CC BY-NC-ND license (http://creativecommons.org/licenses/by-nc-nd/4.0/).

diffraction measurements during tensile deformation to examine the mechanical properties of DSS. Their results indicated that, while the γ phase was responsible for the onset of yielding, the α phase significantly contributed to tensile strength. Additionally, they observed that the contribution of γ to uniform elongation was significant and that a higher volume fraction of γ correlated with increased total elongation. However, in most studies on the deformation behavior of DSS using *in situ* neutron diffraction during tensile testing, the analysis has been limited to lattice strains and phase-averaged strains. Accurate phase stresses and the stress contributions of individual constituent phases to the strength have not been thoroughly evaluated. This limitation is likely due to the significant intergranular stress partitioning in DSS and its strong rolling texture, which complicates analysis. By accurately analyzing phase stress while accounting for texture effects, a more in-depth understanding of the deformation behavior of dual-phase alloys can be achieved.

Furthermore, the deformation behavior of dual-phase alloys is significantly influenced by the mechanical response of each constituent phase. The dependence of strength and ductility on test temperature and strain rate varies with crystal structure. In a low-temperature range below room temperature, the yield stress and tensile strength of the BCC phase increase as temperature decreases [20–22], whereas the yield stress of the FCC phase remains nearly constant, with only a slight increase in tensile strength [23–26]. Consequently, in dual-phase alloys consisting of BCC and FCC phases, the relative strength difference between the constituent phases increases at lower temperatures, resulting in changes in stress partitioning behavior. In the Cu-40 mass% Fe alloy, a representative dual-phase alloy previously studied by our group [27], the strength of the FCC phase remained nearly unchanged at 150 K compared to 293 K, whereas the strength of the BCC phase increased significantly. As a result, the strength difference between the constituent phases became more pronounced at low temperatures. This suggests that test temperature has a significant effect on stress partitioning behavior. Several studies have investigated the deformation behavior of DSSs at low temperatures [28–31]. Tsuchida et al. [29] conducted tensile tests on DSSs containing metastable γ in a temperature range of 123 K–373 K and evaluated their stress-strain response. They found that, in addition to the general trend of increasing strength with decreasing temperature, the highest total elongation was achieved at 258 K due to deformation-induced martensitic transformation (DIMT) of γ. However, it has also been reported that DIMT does not always improve ductility, especially at cryogenic temperatures. In metastable austenitic stainless steels, rapid martensitic transformation occurring at small strains can lead to early strain localization, resulting in a reduction in total elongation [32,33]. These findings suggest that the kinetics of DIMT plays a vital role in determining mechanical properties, and its influence may vary depending on the temperature and phase stability. Koga et al. [30] performed tensile tests on a DSS containing a relatively stable γ in a temperature range of 8 K–293 K to examine their tensile deformation behavior. Their results indicated that strength increased as the temperature decreased, but the total elongation slightly decreased at 200 K, where DIMT did not occur. The total elongation increased again at 77 K due to DIMT. These findings suggest that even in the absence of DIMT, DSS exhibits higher strength at low temperatures compared to room temperature, while maintaining total elongation equivalent to that at room temperature. Based on studies of Cu-Fe alloys [27], this behavior is predicted to result from changes in stress partitioning and the deformation behavior of each constituent phase. However, very few studies have evaluated the stress partitioning behavior in DSS at the low temperature range, and the mechanisms underlying changes in the relative strength difference between the constituent phases, as well as how DSS achieves high strength and ductility without DIMT at low temperatures, remain unclear.

Given these gaps, an accurate evaluation of phase stresses in DSSs and a comprehensive investigation of the mechanisms governing strength and ductility at low temperatures are fundamental for understanding the complex deformation behavior of dual phase alloys. In recent years, Harjo et al. [34] proposed a method for deriving phase stress by accounting for the effect of texture evolution during tensile deformation of magnesium alloy (AZ31) in *in situ* neutron diffraction measurements. Mao et al. [35,36] later applied this method to analyze phase stresses in steels. This approach is expected to provide more reliable phase stress estimations.

The objective of this study is to quantify the phase-specific stress and deformation behaviors of duplex stainless steel at 293 K and 200 K using *in situ* neutron diffraction analysis with texture compensation. In addition, the mechanisms contributing to strength and ductility at low temperatures are discussed. While several studies have investigated phase stress partitioning in duplex stainless steels at room temperature, experimental data under low temperature conditions remain scarce. This study provides new insight into the phase-specific deformation mechanisms at 200 K, which is below room temperature, through texture-compensated *in situ* neutron diffraction analysis—highlighting the respective contributions of ferrite and austenite to the enhanced mechanical performance in a low-temperature environment.

2. Experimental procedures

2.1. Material

The DSS (JIS SUS329J4L, Fe-25Cr-7Ni-3Mo-0.5Si-0.7Mn-0.11N (mass%)) from the same lot used in the previous study [30] was employed. The heat treatment history of this sample is as follows: a commercially available sheet specimen was cold-rolled to achieve a 40 % reduction in thickness, reaching a final thickness of 2.5 mm. Following cold rolling, the material was annealed at 1473 K for 10 min and subsequently air-cooled. It was then held at 1273 K for 30 s to coarsen the grains. The resulting microstructure consisted of two phases, α and γ, with an average grain size of approximately 10 μm for both phases. The grains exhibited a slightly elongated shape in the rolling direction (RD). The phase fractions of α and γ, determined *via* electron backscattered diffraction (EBSD), were nearly equal. A plate-type specimen, shaped as shown in Fig. 1a, was cut from the sheet material, aligning the tensile loading direction (LD) parallel to the RD. The specimen surface was mechanically polished to a grit size of #2400 and subsequently finished by buffing.

2.2. Neutron diffraction

In situ neutron diffraction measurements during tensile testing were performed at 293 K and 200 K using TAKUMI [37], a time-of-flight diffractometer dedicated to the investigation of engineering materials at the MLF of J-PARC. A schematic of the experimental setup is shown in Fig. 1b. During the experiments, the tensile LD was oriented horizontally at 45° relative to the incident neutron beam. Neutron diffraction data for the scattering vector parallel to the LD were collected at the axial detector, while data for the scattering vector perpendicular to the LD (normal direction, ND) were collected at the transverse detector. An incident beam slit of 5 mm (width) × 5 mm (height) was used, and a pair of radial collimators with a viewing width of 5 mm was employed. The neutron diffraction measurements were conducted at a neutron beam power of 300 kW. Fig. 1c presents a photograph of the cooling system equipment [38] used in this study, as shown in the figure. Temperature control was achieved by attaching a thermocouple to the specimen gripping section and continuously monitoring the temperature. The tensile test in the elastic region was conducted under stepwise increasing load control with a 300 s holding time, during which neutron diffraction data were collected. In the plastic region, the test was performed under constant crosshead speed control with an initial strain rate of 1.3×10^{-5} s^{-1}, and neutron diffraction data was extracted at 600 s intervals. The measurements continued until the specimen reached ultimate tensile strength. Macroscopic strain was measured using an extensometer at

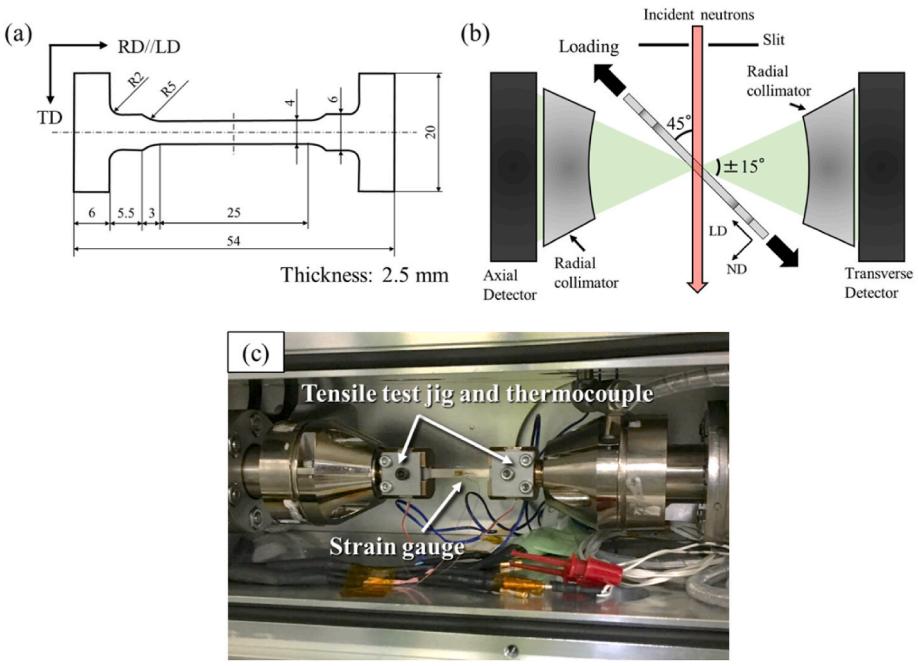

Fig. 1. (a) Geometry of the tensile test specimen used in this study and (b) schematic of experimental setup, and (c) photograph of cooling system equipment of the TAKUMI instrument.

293 K and a strain gauge at 200 K, as shown in Fig. 1c.

2.3. Data analysis

The lattice spacings of several *hkl* planes in the LD and ND were obtained using a single-peak fitting method implemented in the Z-Rietveld software [39]. The *hkl* lattice strains in the LD (ε_i^{hkl}, $i = \alpha$ and γ) were estimated using the following equation:

$$\varepsilon_i^{hkl} = \frac{d_i^{hkl} - d_{i,0}^{hkl}}{d_{i,0}^{hkl}} \quad (1)$$

where, d_i^{hkl} is the lattice spacing of the [*hkl*]//LD grains in the *i* phase during deformation, and $d_{i,0}^{hkl}$ is the reference lattice spacing of the [*hkl*]//LD grains prior to deformation. To minimize the effect of texture evolution during deformation, phase stress (σ_i, $i = \alpha$ and γ) was derived using the method proposed by Mao et al. [35,36]:

$$\sigma_i = \sum_0^m f_i^{hkl} E_i^{hkl} \varepsilon_i^{hkl} \quad (2)$$

$$f_i^{hkl} = \frac{I_i^{hkl}/R_i^{hkl}}{\sum_0^m I_i^{hkl}/R_i^{hkl}} \quad (3)$$

where, f_i^{hkl} represents the phase fraction of [*hkl*]//LD grain in the *i* phase, E_i^{hkl} is the elastic constant of [*hkl*]//LD grain in the *i* phase, I_i^{hkl} is the measured integrated intensities of *hkl*//LD diffraction peaks for the *i* phase, and R_i^{hkl} is the theoretical integrated intensities of *hkl*//LD diffraction peaks of the *i* phase for a completely random texture. The σ_α was evaluated using the 110-α, 200-α, 211-α, and 310-α reflection peaks, while σ_γ was evaluated using the 111-γ, 200-γ, 220-γ, and 311-γ reflection peaks. The same software was used to analyze the full width at half maximum (FWHM) and peak integrated intensities of several *hkl* peaks during tensile deformation. The FWHM values were normalized by their peak position, while the peak integrated intensities were normalized by their initial value (prior to deformation) at each test temperature. The phase fractions before and after deformation were estimated using the Rietveld refinement method available in the same software.

3. Results

3.1. Initial diffraction pattern and tensile properties

Fig. 2a and b shows the diffraction patterns obtained before tensile testing at 293 K and 200 K, respectively. In both specimens, the 110-α//LD, 111-γ//LD, and 200-γ//LD diffraction peaks, which are parallel to the RD were relatively strong, indicating a pronounced rolling texture. The phase fractions of α and γ, obtained from the diffraction patterns, were 53.8 ± 0.5 % and 46.2 ± 0.5 % at 293 K, respectively, and 53.9 ± 0.6 % and 46.1 ± 0.6 % at 200 K. No phase transformation occurred upon cooling to 200 K due to the high stability of γ in DSS.

Fig. 3a and b shows diffraction patterns for the conditions near the tensile strength at 293 K and 200 K, respectively. The diffraction peaks broadened compared to those before tensile testing. At both temperatures, the area of 110-α//LD, 111-γ//LD, and 200-γ//LD reflections became larger due to tensile deformation. The phase fractions of α and γ obtained from diffraction patterns were 54.0 ± 0.8 % and 46.0 ± 0.8 % at 293 K, respectively, and 54.9 ± 1.0 % and 45.1 ± 1.0 % at 200 K. At 293 K, there was almost no change in the phase fractions before and after the tensile test. At 200 K, the γ phase fraction slightly decreased by approximately 1.0 %. However, this change falls within the experimental error margin associated with the phase fraction analysis. Therefore, it can be explicitly stated that the observed change is not statistically significant, and DIMT did not occur. This observation is further supported by the estimated Md_{30} temperature—the temperature at which 50 % of the austenite phase transforms to martensite under 30 % plastic deformation. The Md_{30} value reflects the stability of the γ phase against DIMT. Based on the chemical composition of the investigated material, the Md_{30} temperature was calculated to be approximately 162 K using the empirical formula proposed by Nohara et al. [40], which was originally developed for metastable austenitic stainless steels. Since this value is lower than the test temperature of 200 K, it suggests that the γ phase was sufficiently stable to suppress martensitic transformation under the present deformation conditions. Consequently, in this study, the phase fraction was considered constant during

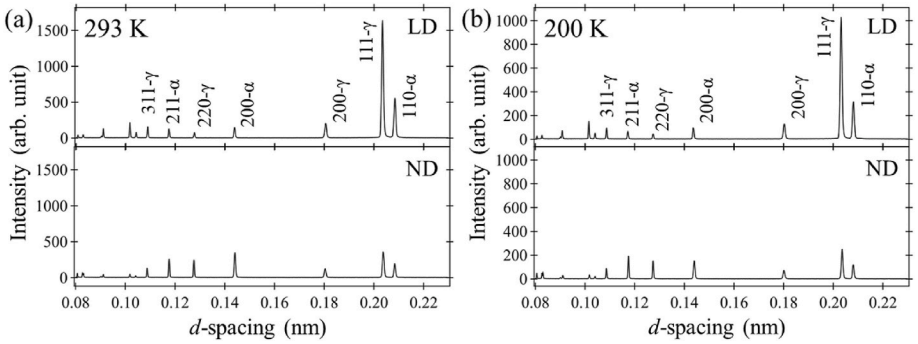

Fig. 2. Diffraction patterns before tensile test for the LD and ND at (a) 293 K and (b) 200 K.

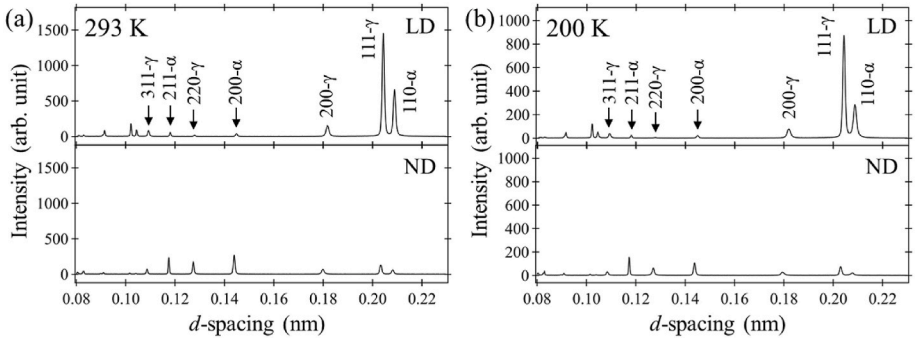

Fig. 3. Diffraction patterns at tensile strength for the LD and ND at (a) 293 K and (b) 200 K.

deformation, with its value set based on the phase fraction before deformation.

Fig. 4a presents the nominal stress-nominal strain curves at 293 K and 200 K. Representative mechanical properties, including the 0.2 % proof stress, tensile strength, and uniform elongation, are summarized in Table 1. At 293 K, the DSS exhibited a uniform elongation of approximately 20 % and a tensile strength of approximately 620 MPa. At 200 K, both the yield stress and tensile strength increased compared to 293 K, while uniform elongation slightly decreased. Fig. 4b shows the work hardening rate and true stress as a function of true strain. At 293 K, the work hardening rate decreased as deformation progressed, with the rate of decrease slowing at around 12 % strain. At 200 K, the work hardening rate was slightly higher than that at 293 K throughout the initial plastic deformation up to approximately 9.7 % strain.

Table 1
Representative mechanical properties of duplex stainless steel at 293 K and 200 K.

Temperature	0.2 % proof stress	Tensile strength	Uniform elongation
293 K	429 MPa	625 MPa	21.4 %
200 K	629 MPa	882 MPa	20.2 %

3.2. Lattice strain and phase stress partitioning behavior

Fig. 5a and b shows the changes in $\varepsilon_{\gamma}^{hkl}$//LD at 293 K and 200 K, plotted against applied true stress. The σ_{E}^{macro} and $\sigma_{0.2}^{macro}$ indicate the macroscopic elastic limit and 0.2 % proof stress, respectively. The variations in $\varepsilon_{\gamma}^{hkl}$ reflect elastic anisotropy. At both temperatures, differences in the increasing slope of $\varepsilon_{\gamma}^{hkl}$ were observed, indicating the onset of a change in the deformation mode. The increase in $\varepsilon_{\gamma}^{111}$ began to slow

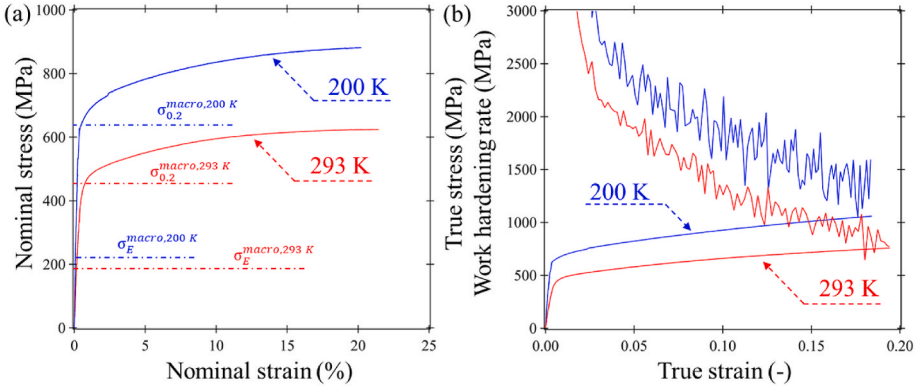

Fig. 4. (a) Nominal stress vs. nominal strain curves and (b) true stress and work hardening rate vs. true strain curves. The σ_{E}^{macro} and $\sigma_{0.2}^{macro}$ in (a) represent the macroscopic elastic limit and 0.2 % proof stress values.

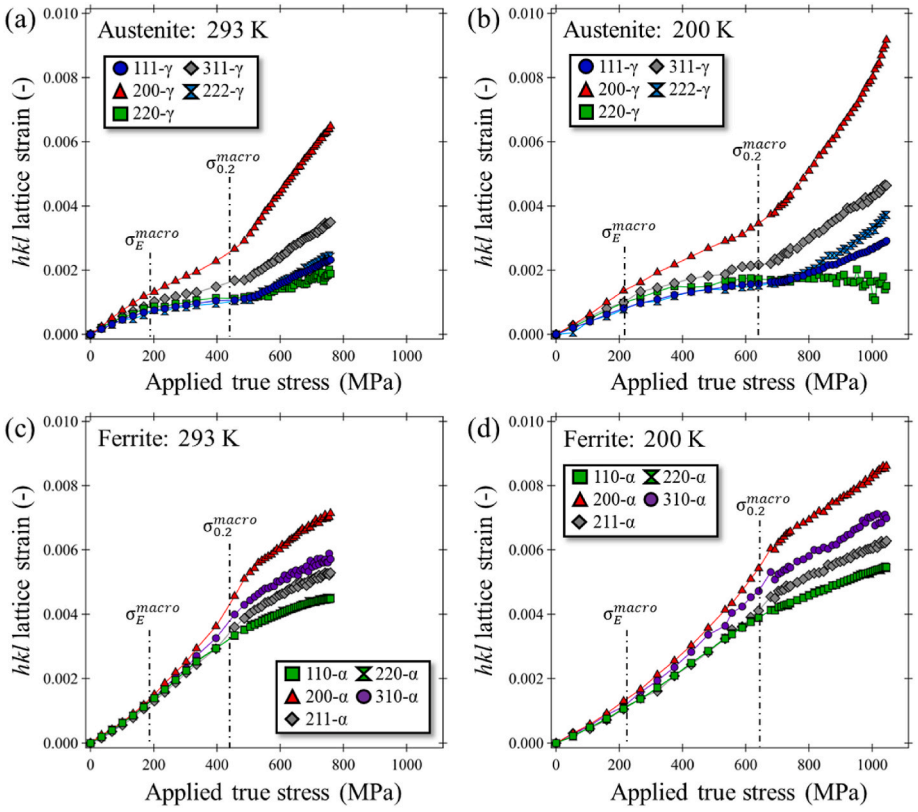

Fig. 5. Changes in the lattice strains as a function of applied true stress. Changes are shown for several *hkl* peaks of γ at (a) 293 K and (b) 200 K, while of α at (c) 293 K and (d) 200 K.

before reaching σ_E^{macro}, followed by other ε_γ^{hkl}, which also gradually slowed beyond σ_E^{macro}. This indicates that the γ phase preferentially yielded to initiate plastic deformation. Subsequently, the increase in ε_γ^{hkl} re-accelerated at a stress slightly above $\sigma_{0.2}^{macro}$. These trends were consistent regardless of test temperature. Among the [*hkl*] family grains, ε_α^{200} exhibited the largest change during deformation, while ε_γ^{111} and ε_γ^{220} showed the smallest. ε_γ^{311} displayed intermediate changes between these values. This suggests that intergranular stress partitioning occurs among the [*hkl*] family grains in the γ phase, likely due to differences in the diffraction elastic constant, the Schmid factor and the plastic deformability. At both temperatures, ε_γ^{311} exhibited lattice strain changes close to the average, which is consistent with empirical findings that ε_γ^{311} typically represents the average lattice strain behavior of the FCC phase [41]. This may indicate that σ_γ value can be reasonably estimated using ε_γ^{311}. Notably, at 200 K, the responses of ε_γ^{111} and ε_γ^{222} after the onset of plastic deformation exhibited a split, with ε_γ^{222} being larger than ε_γ^{111}. Since [111]-γ and [222]-γ grains are principally have the same orientation, their lattice strain values would typically change in a similar manner, as observed at 293 K. This deviation is attributed to the development of stacking faults, a phenomenon also reported in FCC alloys with low stacking fault energy [42–44]. The development behavior of stacking faults in γ is discussed in detail in section 4.1.

Fig. 5c and d shows the changes in ε_α^{hkl}//LD at 293 K and 200 K, plotted against applied true stress. The σ_E^{macro} and $\sigma_{0.2}^{macro}$ represent the macroscopic elastic limit and 0.2 % proof stress values obtained from the stress-strain curves. The variations in the ε_α^{hkl} below $\sigma_{0.2}^{macro}$ reflect mainly elastic anisotropy at each temperature. At 293 K, the increase in ε_α^{hkl} behavior became noticeable once the σ_E^{macro} was exceeded, in response to the slower increase in ε_γ^{hkl} caused by preferential plastic deformation in the γ phase. The increase in ε_α^{110} (and ε_α^{220}) began to slow by reaching $\sigma_{0.2}^{macro}$, followed by other ε_α^{hkl}, which also gradually slowed at a stress level slightly above $\sigma_{0.2}^{macro}$. This indicates that the α phase yielded at this stress level initiating plastic deformation. In response, the increase in ε_γ^{hkl} re-accelerated (Fig. 5a). Among the [*hkl*] family grains, ε_α^{200} exhibited the largest value during deformation, while ε_α^{110} showed the smallest. The ε_α^{211} and ε_α^{310} exhibited intermediate changes between these values. A similar trend was observed at 200 K, with ε_α^{hkl} values higher than those at 293 K. These results suggest that, as in γ, intergranular stress partitioning occurred also in α. Empirically, ε_α^{211} is known to represent average lattice strain changes in the BCC phase [45]. However, in this study, ε_α^{211} values beyond $\sigma_{0.2}^{macro}$ were slightly lower than expected at both temperatures, suggesting that the phase stress calculations relying solely on 211-α//LD diffraction peak may underestimate the actual values.

Fig. 6a presents the change in the σ_α and σ_γ at 293 K and 200 K with respect to the applied true stress. At 293 K, phase stress partitioning between α and γ occurred once the $\sigma_E^{macro,293\ K}$ was exceeded, which was caused by the yielding of γ. Between $\sigma_E^{macro,293\ K}$ and $\sigma_{0.2}^{macro,293\ K}$, the increase in σ_γ slowed, due to the plastic deformation in γ. When macroscopic yielding occurred (at $\sigma_{0.2}^{macro,293\ K}$), the increase in σ_α also became more gradual, indicating that the α phase had also undergone plastic deformation. After that, as deformation progressed, phase stress partitioning between α and γ gradually decreased. A similar trend was observed also at 200 K, where phase stress partitioning between α and γ for $\sigma_{0.2}^{macro,200\ K}$ was larger than that observed at 293 K for $\sigma_{0.2}^{macro,293\ K}$. Regardless of test temperature, the γ phase began to exhibit plastic deformation near σ_E^{macro}, with the stress at which plastic deformation began increasing slightly at 200 K. In contrast, the stress at which the α initiated plastic deformation ($\sigma_{0.2}^{macro}$) was approximately 200 MPa higher at 200 K than at 293 K, suggesting that the yield strength of α was more strongly influenced by temperature than that of γ. Fig. 6b presents the

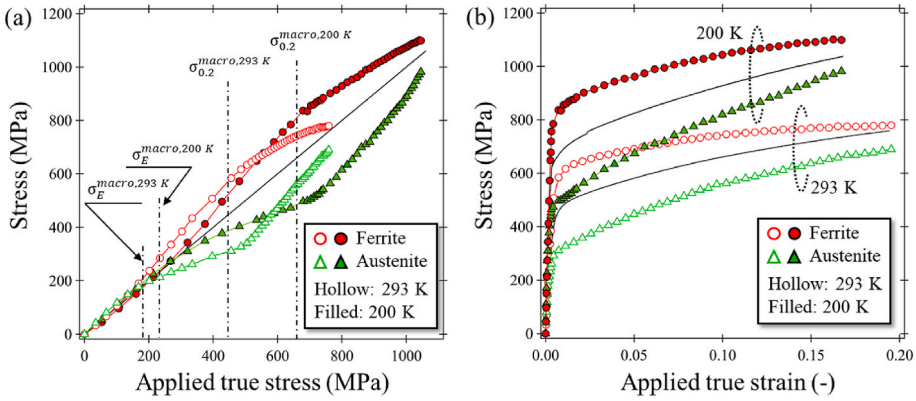

Fig. 6. Changes in phase stresses of α and γ at 293 K and 200 K as a function of (a) applied true stress and (b) applied true strain. Solid black lines in (b) indicate the true stress-true strain curves at both temperatures.

change in σ_α and σ_γ at 293 K and 200 K as a function of applied true strain. At both temperatures, σ_α was higher than σ_γ. As the temperature decreased, both σ_α and σ_γ increased compared to 293 K. In γ, the increase in σ_γ with respect to the true strain became more pronounced at 200 K, suggesting an enhancement in its work hardening. Similarly, in α, the increase in σ_α with respect to true strain was greater at 200 K than at 293 K, indicating an increase in its work hardening as well. Although the increase in yield stress and tensile strength was larger in α than in γ, the enhancement in work hardening was more pronounced in γ.

3.3. Contribution of constituent phases to the strength

The stress contributions of constituent phases to strength (σ_α^{cont} and σ_γ^{cont}) were evaluated by weighting the phase stresses, calculated using Eq. (2), by the phase fractions. Fig. 7a and b shows the σ_α^{cont} and σ_γ^{cont} at 293 K and 200 K as a function of applied true strain. The black solid line represents the true stress-true strain curve obtained from tensile testing, while the bar length in the figure indicates the stress contribution of each phase. At both temperatures, the sum of σ_α^{cont} and σ_γ^{cont} was approximately equal to the applied true stress. This indicates that stress equilibrium was satisfied, where the applied true stress equaled the sum of σ_α^{cont} and σ_γ^{cont}. These results suggest that the phase stresses were accurately estimated at both temperatures. However, at 293 K, a slight deviation was observed between the sum of σ_α^{cont} and σ_γ^{cont} and the applied true stress in the later stages of deformation (>15 % strain). The cause of this discrepancy remains unclear and is a subject for future investigation.

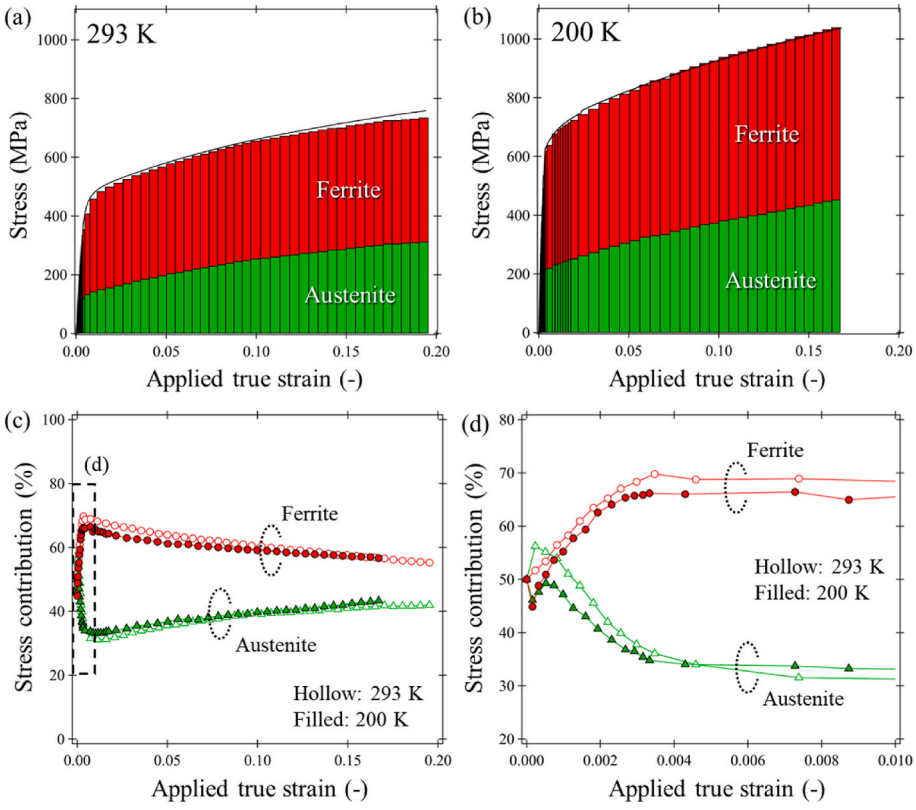

Fig. 7. Fraction-weighted phase stresses and stress contributions. The sum of stresses contributed by α and γ during tensile testing at (a) 293 K and (b) 200 K. (c) Stress contribution to the strength of α and γ. (d) close-up view of the range up to 1 % strain in (c). The stress contributions were obtained by normalizing the contributed stresses with the applied true stresses.

Fig. 7c illustrates the percentage contributions of α and γ to strength as a function of true strain, while Fig. 7d provides a close-up view of the range up to 1 % strain. At both temperatures, α contributed more to the strength than γ. The increase in σ_{α}^{cont} accompanied by the decrease in σ_{γ}^{cont} can be attributed to the preferential plastic deformation occurring in the γ phase at the beginning of tensile loading. Within the range up to 0.2 % strain, the sum of stress contributions from α and γ exceeded 100 % at 293 K, resulting in an overestimation of the fraction-weighted phase stress. However, while the data show a difference in stress contribution between 293 K and 200 K in the range up to macroscopic yielding, this is likely an artifact of the analysis caused by the transition from elastic to plastic deformation, which affects the accuracy of stress partitioning evaluation in the early stage of deformation. At strains of 0.5 % or more, the stress contribution of α was higher and that of γ was lower at 293 K than at 200 K. However, as the deformation progressed and the strain reached approximately 5 % or more, the stress contribution of each phase became nearly identical at both temperatures, despite the greater increase in work hardening at 200 K compared to 293 K. In our previous *in situ* neutron diffraction study on Cu-Fe alloys during low-temperature tensile deformation [27], work hardening slightly increased in the FCC phase, whereas that in the BCC phase remained nearly unchanged. However, the strength of the BCC phase increased significantly. In the DSS used in this study, the strength and work hardening of both α and γ increased at 200 K. As a result, the proportion of stress contribution from both phases remained similar regardless of temperature.

These findings indicate that the α phase was the larger contributor to the strength of DSS in this study. The increase in strength at 200 K can be attributed to the strengthening and enhanced work hardening of both phases. Additionally, it is noteworthy that the stress contribution of α and γ in the later stage of deformation were nearly identical, irrespective of the test temperature.

4. Discussion

4.1. Deformation mechanism of austenite

Fig. 6b shows that the increase in strength (work hardening) of γ during deformation was more pronounced at 200 K. This increase in strength at lower temperatures is possibly due to dislocation migration becoming more active as the deformation temperature decreases. Additionally, factors influencing the increase in work hardening of γ were assessed.

One potential factor contributing to work hardening is the development of stacking faults. It has been reported that CrMnFeCoNi, an FCC-based high-entropy alloy with low stacking fault energy, exhibits a significant increase in work hardening at cryogenic temperatures [42,43]. This phenomenon has been attributed to the substantial formation of stacking faults during deformation. The split between $\varepsilon_{\gamma}^{111}$ and $\varepsilon_{\gamma}^{222}$ at 200 K, observed in Fig. 5d, is attributed to the development of stacking faults. In DSS, the stacking fault energy of the γ phase is known to be very low, approximately 10 mJ/m^2 [46]. Therefore, in the γ phase of the DSS used in this study, it is possible that the decrease in temperature promoted the formation of stacking faults, leading to an increase in work hardening.

To further evaluate stacking fault formation in this study, the stacking fault probability (SFP) in FCC was estimated using the following equation, provided by Warren [47], based on changes in $\varepsilon_{\gamma}^{111}$ and $\varepsilon_{\gamma}^{222}$.

$$SFP = \frac{32\pi}{3\sqrt{3}}\left(\varepsilon_{\gamma}^{222} - \varepsilon_{\gamma}^{111}\right) \quad (4)$$

The SFP value calculated from Eq. (4) represents the number of stacking faults per 1000 atoms.

Fig. 8 illustrates the changes in SFP at 293 K and 200 K as a function of applied true stress. At 293 K, the development of stacking faults was minimal, contributing only slightly to work hardening. In contrast, at 200 K, SFP continued to increase with increasing applied true stress after macroscopic yielding. Near the tensile strength, the amount of stacking faults was approximately three times higher than at 293 K. These results suggest that the development of stacking faults significantly contributed to the increase in work hardening of γ at 200 K, as shown in Fig. 6b.

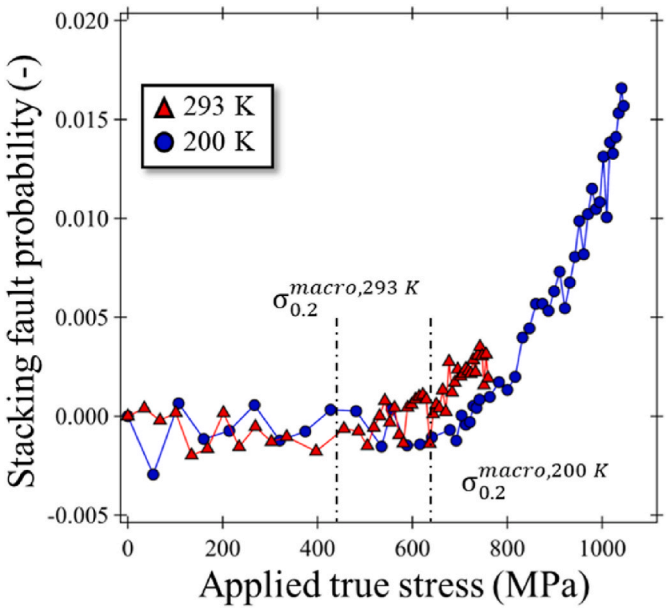

Fig. 8. Changes in stacking fault probability (SFP) of γ at 293 K and 200 K as a function of applied true stress.

The formation of stacking faults is a precursor to major deformation mechanisms such as deformation twinning and phase transformation. Therefore, it is possible that DIMT and deformation twinning also contribute to the increase in the work hardening of γ. Meanwhile, the change in the γ phase fraction during plastic deformation at 200 K was minimal in this study, suggesting that phase transformation did not occur in the uniform deformation region. Thus, the contribution of DIMT can be considered negligible. A qualitative evolution of deformation twinning can be conducted by examining changes in the relative integrated intensities of 111-γ and 200-γ (I_{γ}^{111} and I_{γ}^{200}). In FCC alloys under uniaxial tension, the peak integrated intensities of 111-γ//LD and 200-γ//LD typically increase monotonically with applied stress or strain. A previous study [48] has shown that when deformation twins actively form, the proportion of [111]-γ//LD and [200]-γ//LD grains decreases and increases, respectively. Consequently, the slope of I_{γ}^{111} decreases, while the slope of I_{γ}^{200} increases. If twinning deformation were promoted at low temperatures, deviations in the trend of increasing relative integrated intensities during deformation should be observed. Fig. 9a presents the change in the I_{γ}^{111} and I_{γ}^{200} at 293 K and 200 K as a function of applied true stress. At 293 K, both intensities increased linearly with increasing applied true stress. At 200 K, a similar linear increase was observed, with no significant deviation from the trend at 293 K. In high-entropy alloys [39,41], the increase in the relative integrated intensity of 111-γ has been reported to nearly plateau at high applied stress above 2000 MPa, where stacking faults and twins become prominent during deformation at 15 K. Likewise, in twinning induced plasticity (TWIP) steel [49], where twinning is known to be active, the rate of increase in the relative integrated intensities of 111-γ and 200-γ slows down at low temperatures. In contrast, our results showed no marked difference in the increasing trends of I_{γ}^{111} and I_{γ}^{200} between 293 K and 200 K. These observations suggest that twinning deformation had little influence on the enhancement of work hardening of γ.

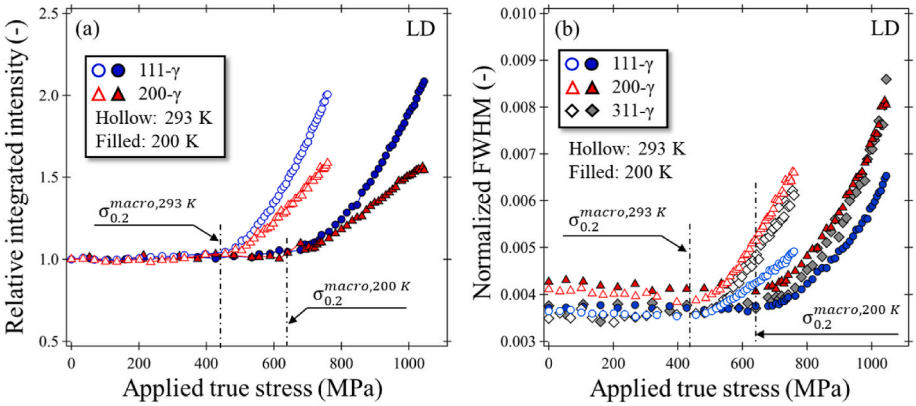

Fig. 9. Changes in (a) the relative integrated intensities of 111-γ and 200-γ and (b) the FWHM of several *hkl* peaks at 293 K and 200 K.

From these findings, it is inferred that the increase in work hardening of γ at 200 K was primarily due to the development of stacking faults in addition to the activity of dislocation migration, while the contribution of twinning deformation was minimal.

Fig. 9b shows the normalized FWHM of representative γ peaks as a function of applied true stress. The FWHM of γ increased after macroscopic yielding, with its value significantly higher at 200 K than at 293 K. In general, the increase in FWHM value by deformation is known to correlate with the increase in dislocation density [36,50–52]. A previous study reported that in the VCoNi alloy, which consists of a single-phase FCC structure, strength and ductility can be enhanced at low temperatures even without the formation of stacking faults, due to increased dislocation activity [50]. The dislocation density in VCoNi alloy, near its tensile strength, increases from approximately 7.5×10^{15} m^{-2} to 12.5×10^{15} m^{-2} —a factor of less than 1.7— when the deformation temperature is lowered from 293 K to 15 K (a temperature difference of 278 K). Thus, the increase in FWHM of γ at 200 K compared to 293 K in this study may be too large to be attributed solely to dislocation migration activity. As previously described, the formation of stacking faults accompanied the deformation of DSS at 200 K in this study. The presence of stacking faults also influences the FWHM [53,54]. Therefore, the large increase in FWHM of γ at 200 K is likely due to the development of stacking faults in addition to dislocation accumulation.

The changes in normalized FWHM and relative integrated intensities of γ at 200 K suggest that both the dislocation activity and the stacking fault development in γ increase at low temperatures. Therefore, in addition to the improvement in work hardening due to the enhanced dislocation activity, it is considered that the stacking fault development also contributes to the increased strength and work hardening of γ at 200 K.

4.2. Deformation mechanism of ferrite

At 200 K, not only the yield strength but the work hardening of α increased also significantly. Fig. 10a shows the normalized FWHM of representative α peaks as a function of applied true stress. The FWHM of α increased after macroscopic yielding at both temperatures. At 200 K, the FWHM values of α near the tensile strength were higher than that at 293 K. Since the increase in FWHM value by deformation can be correlated to the increase in dislocation density, the observed changes in FWHM of α after exceeding $\sigma_{0.2}^{macro}$ in this study are considered to be associated with the accumulation of dislocations.

In general, the strength of BCC phase increases significantly at low temperatures, whereas elongation and work hardening tend to decrease [22,55]. A previous study has reported that work hardening is greatly enhanced in a BCC-based alloy when martensite with a hexagonal close-packed (HCP) structure forms during deformation [56]. However, since DIMT did not occur in this study, its effect can be considered negligible. Additionally, a previous study has shown that martensitic steel exhibits plastic deformation despite a significant increase in strength at low temperatures [57]. This suggests that dislocation migration in BCC phase occurs sufficiently even at low temperatures. Therefore, it is likely that the plastic deformation behavior of α due to dislocation glide also occurred at 200 K in this study.

Next, to evaluate changes in the crystal orientation of α, the relative integrated intensity of 110-α (I_{α}^{110}) was examined. It should be noted that [110]-α//LD represents the primary orientation of the tensile texture in the BCC phase. If FWHM accurately reflects dislocation density, an increase in crystal rotation with dislocation glide should correspond to a higher relative integrated intensity at lower temperatures. Fig. 10b shows the change in I_{α}^{110} at 293 K and 200 K as a function of applied true stress. At both temperatures, I_{α}^{110} increased after macroscopic yielding,

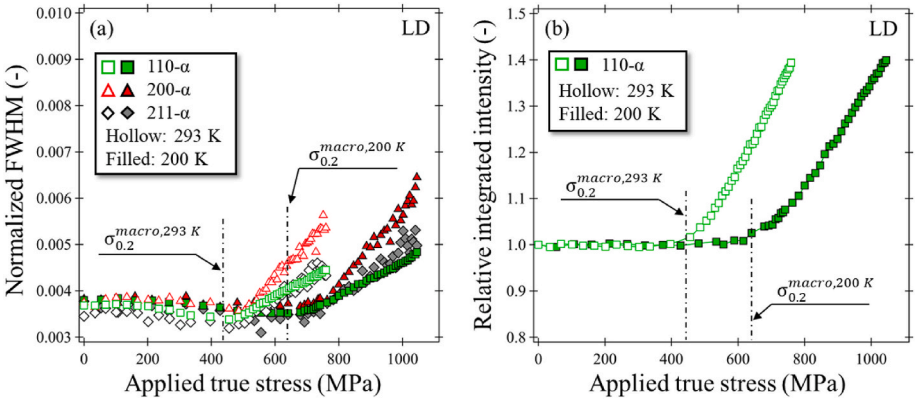

Fig. 10. Changes in (a) the FWHM of several *hkl* peaks and (b) the relative integrated intensity of 110-α at 293 K and 200 K as a function of applied true stress.

indicating the development of a tensile texture. The rate of increase in I_{α}^{110} was slightly higher at 293 K than at 200 K, but near the tensile strength, the I_{α}^{110} was nearly the same at both temperatures. Therefore, it is inferred that the amount of dislocation glide remained largely unchanged, suggesting that FWHM roughly reflects dislocation density. Screw-type dislocations are mainly found in BCC polycrystalline materials [58,59]. Screw dislocations can move in any direction and therefore are annihilated relatively easily, even when they are far apart from each other [60]. Therefore, Fig. 10a may suggest that lowering the deformation temperature reduces the likelihood of dislocation annihilation, allowing dislocation accumulation to occur more effectively.

Given these findings, two possible factors may account for the improvement in the work hardening of α at 200 K:

(1) At low temperatures, dislocation accumulation in α was more efficient due to the suppression of dislocation recovery.
(2) Dynamic grain refinement in γ, which occurs when stacking faults form, leads to hardening. The strengthening of γ limits stress redistribution, thereby increasing load on α.

To further elucidate the work hardening mechanism at low temperatures, a detailed investigation of the low temperature deformation behavior of DSS with different stacking fault energies and grain sizes is necessary. This remains an important topic for future research.

5. Conclusions

In this study, *in situ* neutron diffraction measurements were conducted during tensile tests at 293 K and 200 K on DSS. To accurately evaluate the phase stresses and the stress contributions of each constituent phase to the strength, phase stresses were derived using a method that accounted for the effect of texture. Additionally, changes in the deformation mechanisms of each phase at 200 K were examined. The main findings are summarized as follows:

(1) At 200 K, the macroscopic yield stress and tensile strength increased significantly compared to 293 K, while uniform elongation remained nearly unchanged. The work hardening rate at 200 K was higher than that at 293 K.
(2) At both temperatures, intergranular stress partitioning was clearly observed in α once the elastic limit was exceeded, whereas in γ, intergranular stress partitioning occurred near the elastic limit. Phase stress partitioning occurred upon exceeding the elastic limit, regardless of temperature.
(3) By estimating phase stress while considering texture, the stress equilibrium was satisfied, where the sum of the phase stresses weighted by their phase fractions was equal to the applied true stress. This approach allowed for a more reliable evaluation of phase stress partitioning behavior and the stress contribution to strength.
(4) No martensitic transformation was observed in the tested temperature range, indicating that the observed changes in strength and deformation behavior were not due to with phase transformation but were instead associated with differences in stress partitioning and dislocation-based mechanisms.
(5) The stress contribution of α to strength was higher than that of γ at both temperatures. The proportion of contribution from each constituent phase showed no significant variation with temperature.
(6) At 200 K, both the strength and work hardening of α and γ increased. The enhancement of work hardening in γ at 200 K was attributed to the development of stacking faults, along with increased dislocation activity. In contrast, for α, it was suggested that the enhancement resulted from more efficient dislocation accumulation and the strengthening of the γ phase at lower temperature. These findings indicate that the combination of strengthening and enhanced work hardening in both phases contributed to the high strength of DSS at 200 K while maintaining ductility similar to that at 293 K.

CRediT authorship contribution statement

Takayuki Yamashita: Writing – review & editing, Writing – original draft, Visualization, Project administration, Investigation, Funding acquisition, Formal analysis, Data curation, Conceptualization. **Norimitsu Koga:** Writing – review & editing, Visualization, Investigation, Funding acquisition, Conceptualization. **Mao Wenqi:** Writing – review & editing, Visualization, Methodology, Investigation. **Wu Gong:** Writing – review & editing, Visualization, Methodology, Investigation. **Takuro Kawasaki:** Writing – review & editing, Visualization, Resources, Methodology, Investigation. **Stefanus Harjo:** Writing – review & editing, Visualization, Project administration, Methodology, Investigation, Funding acquisition. **Hidetoshi Fujii:** Writing – review & editing, Supervision, Project administration, Funding acquisition. **Osamu Umezawa:** Writing – review & editing, Supervision, Resources, Project administration, Conceptualization.

Declaration of competing interest

The authors declare that they have no known competing financial interests or personal relationships that could have appeared to influence the work reported in this paper.

Acknowledgements

The authors would like to express his sincere thanks to Mr. Tatsuya Nameki (Yokohama National University) for providing the heat-treated sample. This study received financial support from the Project on Design & Engineering by Joint Inverse Innovation for Materials Architecture (DEJI^{2}MA) from the Ministry of Education, Culture, Sports, Science and Technology (MEXT) and the Japan Society for the Promotion of Science (grant No. 24K08099, 25K03397), MEXT Program: Data Creation and Utilization Type Material Research and Development (JPMXP1122684766). The neutron diffraction experiments were performed at BL19 in the Materials and Life Science Experimental Facility of J-PARC (proposal No. 2016P0200).

Data availability

No data was used for the research described in the article.

References

[1] M. Sarwar, R. Priestner, Influence of ferrite-martensite microstructural morphology on tensile properties of dual-phase steel, J. Mater. Sci. 31 (1996) 2091–2095, https://doi.org/10.1007/BF00356631.
[2] K. Sugimoto, N. Usui, M. Kobayashi, S. Hashimoto, Effects of volume fraction and stability of retained austenite on ductility of TRIP-aided dual-phase steels, ISIJ Int. 32 (1992) 1311–1318, https://doi.org/10.2355/isijinternational.32.1311.
[3] N. Koga, W. Zhang, S. Tomono, O. Umezawa, Microstructure and low temperature tensile properties in Cu–50 mass%fe alloy, Mater. Trans. 62 (2021) 57–61, https://doi.org/10.2320/matertrans.MT-M2020260.
[4] R. Francis, G. Byrne, Duplex stainless steels—alloys for the 21st century, Metals 11 (2021) 836, https://doi.org/10.3390/met11050836.
[5] M. Ojima, Y. Adachi, Y. Tomota, K. Ikeda, T. Kamiyama, Y. Katada, Work hardening mechanism in high nitrogen austenitic steel studied by in situ neutron diffraction and in situ electron backscattering diffraction, Mater. Sci. Eng. A 527 (2009) 16–24, https://doi.org/10.1016/j.msea.2009.07.066.
[6] M. Ojima, J. Inoue, S. Nambu, P. Xu, K. Akita, H. Suzuki, T. Koseki, Stress partitioning behavior of multilayered steels during tensile deformation measured by in situ neutron diffraction, Scr. Mater. 66 (2012) 139–142, https://doi.org/10.1016/j.scriptamat.2011.10.018.
[7] P. Tao, J-m. Gong, Y-f. Wang, Y. Jiang, Y. Li, W-w. Cen, Characterization on stress-strain behavior of ferrite and austenite in a 2205 duplex stainless steel based on nanoindentation and finite element method, Results Phys. 11 (2018) 377–384, https://doi.org/10.1016/j.rinp.2018.06.023.

[8] S. Li, T. Wang, Q. Tan, R. Li, Y. Wang, X. Wang, Y. Ren, Y. Wang, A brittle fracture mechanism in thermally aged duplex stainless steels revealed by in situ high-energy X-ray diffraction, Mater. Sci. Eng. A 739 (2019) 264–271, https://doi.org/10.1016/j.msea.2018.10.025.
[9] C. Örnek, D.L. Engelberg, An experimental investigation into strain and stress partitioning of duplex stainless steel using digital image correlation, X-ray diffraction and scanning kelvin probe force microscopy, J. Strain Anal. Eng. Des. 51 (2016) 207–219, https://doi.org/10.1177/0309324716631669.
[10] N. Tsuchida, T. Kawahata, E. Ishimaru, A. Takahashi, H. Suzuki, T. Shobu, Static tensile deformation behavior of a lean duplex stainless steel studied by in situ neutron diffraction and synchrotron radiation white X-rays, ISIJ Int. 53 (2013) 1260–1267, https://doi.org/10.2355/isijinternational.53.1260.
[11] Y. Zhao, L.L. Joncour, A. Baczmański, S. Wroński, B. Panicaud, M. François, C. Braham, T. Buslaps, Stress distribution correlated with damage in duplex stainless steel studied by synchrotron diffraction during plastic necking, Mater. Des. 113 (2017) 157–168, https://doi.org/10.1016/j.matdes.2016.10.014.
[12] Y. Tian, S. Lin, J.Y.P. Ko, U. Lienert, A. Borgenstam, P. Hedström, Micromechanics and microstructure evolution during in situ uniaxial tensile loading of TRIP-assisted duplex stainless steels, Mater. Sci. Eng. A 734 (2018) 281–290, https://doi.org/10.1016/j.msea.2018.07.040.
[13] R. Dakhlaoui, A. Baczmański, C. Braham, S. Wroński, K. Wierzbanowski, E. C. Oliver, Effect of residual stresses on individual phase mechanical properties of austeno-ferritic duplex stainless steel, Acta Mater. 54 (2006) 5027–5039, https://doi.org/10.1016/j.actamat.2006.06.035.
[14] A. Baczmański, Y. Zhao, E. Gadalińska, L.L. Joncour, S. Wroński, C. Braham, B. Panicaud, M. François, T. Buslaps, K. Soloducha, Elastoplastic deformation and damage process in duplex stainless steels studied using synchrotron and neutron diffractions in comparison with a self-consistent model, Int. J. Plast. 81 (2016) 102–122, https://doi.org/10.1016/j.ijplas.2016.01.018.
[15] P. Hou, Y. Li, D. Chae, Y. Ren, K. An, H. Choo, Lean duplex TRIP steel: role of ferrite in the texture development, plastic anisotropy, martensitic transformation kinetics, and stress partitioning, Materials 15 (2021) 100952, https://doi.org/10.1016/j.mtla.2020.100952.
[16] A. Matsushita, N. Tsuchida, E. Ishimaru, N. Hirakawa, W. Gong, S. Harjo, Effects of loading direction on the anisotropic tensile properties of duplex stainless steels based on phase strains obtained by in situ neutron diffraction experiments, J. Mater. Eng. Perform. 33 (2024) 6352–6361, https://doi.org/10.1007/s11665-023-08424-0.
[17] S. Morooka, N. Sato, M. Ojima, S. Harjo, Y. Adachi, Y. Tomota, O. Umezawa, In-situ neutron diffraction study on work-hardening behavior in a ferrite-martensite dual phase steel, Int. J. Automot. Eng. 2 (2011) 131–136, https://doi.org/10.20485/jsaeijae.2.4_131.
[18] S. Harjo, N. Tsuchida, J. Abe, W. Gong, Martensite phase stress and the strengthening mechanism in TRIP steel by neutron diffraction, Sci. Rep. 7 (2017) 15149, https://doi.org/10.1038/s41598-017-15252-5.
[19] T. Yamashita, S. Morooka, W. Gong, T. Kawasaki, S. Harjo, T. Hojo, Y. Okitsu, H. Fujii, Role of retained austenite and deformation-induced martensite in 0.15C-5Mn steel monitored by in-situ neutron diffraction measurement during tensile deformation, ISIJ Int. 64 (2024) 2051–2060, https://doi.org/10.2355/isijinternational.ISIJINT-2024-196.
[20] T. Takeuchi, Temperature dependence of work-hardening rate in iron single crystals, J. Phys. Soc. Jpn. 26 (1969) 354–362, https://doi.org/10.1143/JPSJ.26.354.
[21] T. Yamashita, S. Morooka, S. Harjo, T. Kawasaki, N. Koga, O. Umezawa, Role of retained austenite in low alloy steel at low temperature monitored by neutron diffraction, Scr. Mater. 177 (2020) 6–10, https://doi.org/10.1016/j.scriptamat.2019.10.002.
[22] M. Tanaka, S. Yamasaki, T. Morikawa, Temperature dependence of the yield stress in TiZrNbHfTa body-centred cubic high-entropy alloy, Mater. Sci. Eng. A 871 (2023) 144917, https://doi.org/10.1016/j.msea.2023.144917.
[23] S. Curtze, V.-T. Kuokkala, Dependence of tensile deformation behavior of TWIP steels on stacking fault energy, temperature and strain rate, Acta Mater. 58 (2010) 5129–5141, https://doi.org/10.1016/j.actamat.2010.05.049.
[24] Z. Wu, H. Bei, G.M. Pharr, E.P. George, Temperature dependence of the mechanical properties of equiatomic solid solution alloys with face-centered cubic crystal structures, Acta Mater. 81 (2014) 428–441, https://doi.org/10.1016/j.actamat.2014.08.026.
[25] D.C.C. Magalhães, A.M. Kliauga, M. Ferrante, V.L. Sordi, Plastic deformation of FCC alloys at cryogenic temperature: the effect of stacking-fault energy on microstructure and tensile behaviour, J. Mater. Sci. 52 (2017) 7466–7478, https://doi.org/10.1007/s10853-017-0979-8.
[26] C. Zheng, W. Yu, Effect of low-temperature on mechanical behavior for an AISI 304 austenitic stainless steel, Mater. Sci. Eng. A 710 (2018) 359–365, https://doi.org/10.1016/j.msea.2017.11.003.
[27] T. Yamashita, N. Koga, T. Kawasaki, S. Morooka, S. Tomono, O. Umezawa, S. Harjo, Work hardening behavior of dual phase copper–iron alloy at low temperature, Mater. Sci. Eng. A 819 (2021) 141509, https://doi.org/10.1016/j.msea.2021.141509.
[28] J. He, G. Han, S. Fukuyama, K. Yokogawa, Tensile behaviour of duplex stainless steel at low temperatures, Mater. Sci. Technol. 15 (1999) 909–920, https://doi.org/10.1179/026708399101506715.
[29] N. Tsuchida, T. Kawahata, E. Ishimaru, A. Takahashi, Effects of temperature and strain rate on tensile properties of a lean duplex stainless steel, ISIJ Int. 54 (2014) 1971–1977, https://doi.org/10.2355/isijinternational.54.1971.
[30] N. Koga, T. Nameki, O. Umezawa, V. Tschan, K.-P. Weiss, Tensile properties and deformation behavior of ferrite and austenite duplex stainless steel at cryogenic temperatures, Mater. Sci. Eng. A 801 (2021) 140442, https://doi.org/10.1016/j.msea.2020.140442.
[31] N. Koga, M. Noguchi, C. Watanabe, Low-temperature tensile properties, deformation and fracture behaviors in the ferrite and austenite duplex stainless steel with various grain sizes, Mater. Sci. Eng. A 880 (2023) 145354, https://doi.org/10.1016/j.msea.2023.145354.
[32] G. Cios, T. Tokarski, A. Żywczak, R. Dziurka, M. Stępień, Ł. Gondek, M. Marciszko, B. Pawłowski, K. Wieczerzak, P. Bała, The investigation of strain-induced martensite reverse transformation in AISI 304 austenitic stainless steel, Metall, Mater. Trans. A 48 (2017) 4999–5008, https://doi.org/10.1007/s11661-017-4228-1.
[33] M.J. Sohrabi, H. Mirzadeh, S. Sadeghpour, R. Mahmudi, A. Kalhor, K. Rodak, H. S. Kim, Remarkable cryogenic strength and ductility of AISI 904L superaustenitic stainless steel: a comparative study, Metall. Mater. Trans. A 55 (2024) 4310–4317, https://doi.org/10.1007/s11661-024-07590-7.
[34] S. Harjo, W. Gong, T. Kawasaki, Stress evaluation method by neutron diffraction for HCP-structured magnesium alloy, Quantum. Beam. Sci. 7 (2023) 32, https://doi.org/10.3390/qubs7040032.
[35] W. Mao, S. Gao, W. Gong, S. Harjo, T. Kawasaki, N. Tsuji, Quantitatively evaluating the huge lüders band deformation in an ultrafine grain stainless steel by combining in situ neutron diffraction and digital image correlation analysis, Scr. Mater. 235 (2023) 115642, https://doi.org/10.1016/j.scriptamat.2023.115642.
[36] W. Mao, S. Gao, W. Gong, Y. Bai, S. Harjo, M.-H. Park, A. Shibata, N. Tsuji, Quantitatively evaluating respective contribution of austenite and deformation-induced martensite to flow stress, plastic strain, and strain hardening rate in tensile deformed TRIP steel, Acta Mater. 256 (2023) 119139, https://doi.org/10.1016/j.actamat.2023.119139.
[37] S. Harjo, T. Ito, K. Aizawa, H. Arima, J. Abe, A. Moriai, T. Iwahashi, T. Kamiyama, Current status of engineering materials diffractometer at J-PARC, Mater. Sci. Forum 681 (2011) 443–448. https://doi.org/10.4028/www.scientific.net/MSF.681.443.
[38] S. Harjo, K. Aizawa, T. Kawasaki, T. Nakamoto, T. Henmi, T. Iwahashi, Cryogenic loading devices for materials science & engineering studies at J-PARC, in: T. Oku, M. Nakamura, K. Sakai, M. Teshigawara, H. Hatsumoto, M. Yonemura, et al. (Eds.), Proceedings of the 21st Meeting of the International Collaboration on Advanced Neutron Sources, 2016, pp. 441–447, https://doi.org/10.11484/jaea-conf-2015-002. Ibaraki, Japan.
[39] R. Oishi, M. Yonemura, Y. Nishimaki, S. Torii, A. Hoshikawa, T. Ishigaki, T. Morishima, K. Mori, T. Kamiyama, Rietveld analysis software for J-PARC, Nucl. Instrum. Methods Phys. Res. 600 (2009) 94–96, https://doi.org/10.1016/j.nima.2008.11.056.
[40] K. Nohara, Y. Ono, N. Ogirima, Composition and grain size dependence of strain-induced martensitic transformation in metastable austenitic stainless steels, Tetsu-to-Hagané 63 (1977) 772–782, https://doi.org/10.2355/tetsutohagane1955.63.5_772 (in Japanese).
[41] B. Clausen, T. Lorentzen, M.A.M. Bourke, M.R. Daymond, Lattice strain evolution during uniaxial tensile loading of stainless steel, Mater. Sci. Eng. A 259 (1999) 1–24, https://doi.org/10.1016/S0921-5093(98)00878-8.
[42] M. Naeem, H. He, F. Zhang, H. Hung, S. Harjo, T. Kawasaki, B. Wang, S. Lan, Z. Wu, F. Wang, Y. Wu, Z. Liu, Z. Zhang, C.T. Liu, X.-L. Wang, Cooperative deformation in high-entropy alloys at ultralow temperatures, Sci. Adv. 6 (2020) eaax4002, https://doi.org/10.1126/sciadv.aax4002.
[43] H. He, M. Naeem, F. Zhang, Y. Zhao, S. Harjo, T. Kawasaki, B. Wang, X. Wu, S. Lan, Z. Wu, W. Yin, Y. Wu, Z. Lu, J.-J. Kai, C.-T. Liu, X.-L. Wang, Stacking fault driven phase transformation in CrCoNi medium entropy alloy, Nano Lett. 21 (2021) 1419–1426, https://doi.org/10.1021/acs.nanolett.0c04244.
[44] W. Woo, J.S. Jeong, D.-K. Kim, C.M. Lee, S.-H. Choi, J.-Y. Suh, S.Y. Lee, S. Harjo, T. Kawasaki, Stacking fault energy analyses of additively manufactured stainless steel 316L and CrCoNi medium entropy alloy using in situ neutron diffraction, Sci. Rep. 10 (2020) 1350, https://doi.org/10.1038/s41598-020-58273-3.
[45] A.P. Druschitz, R.E. Aristizabal, E. Druschitz, C.R. Hubbard, T.R. Watkins, L. Walker, M. Ostrander, In situ studies of intercritically austempered ductile iron using neutron diffraction, Metall. Mater. Trans. 43 (2012) 1468–1476, https://doi.org/10.1007/s11661-011-0921-7.
[46] W. Reick, M. Pohl, A.F. Padilha, Determination of stacking fault energy of austenite in a duplex stainless steel, Steel Res. 67 (1996) 253–256, https://doi.org/10.1002/srin.199605486.
[47] B.E. Warren, X-Ray Diffraction, Dover Publications, New York, 1990.
[48] T. Ito, Y. Ogawa, W. Gong, W. Mao, T. Kawasaki, K. Okada, A. Shibata, S. Harjo, Role of solute hydrogen on mechanical property enhancement in Fe–24Cr–19Ni austenitic steel: an in situ neutron diffraction study, Acta Mater. 287 (2025) 120767, https://doi.org/10.1016/j.actamat.2025.120767.
[49] L. Tang, L. Wang, M. Wang, H. Liu, S. Kabra, Y. Chiu, B. Cai, Synergistic deformation pathways in a TWIP steel at cryogenic temperatures: in situ neutron diffraction, Acta Mater. 200 (2020) 943–958, https://doi.org/10.1016/j.actamat.2020.09.075.
[50] M. Naeem, Y. Ma, J. Tian, H. Kong, L. Romero-Resendiz, Z. Fan, F. Jiang, W. Gong, S. Harjo, Z. Wu, X.-L. Wang, Unusual low-temperature ductility increase mediated by dislocations alone, Mater. Sci. Eng. A 924 (2025) 147819, https://doi.org/10.1016/j.msea.2025.147819.
[51] A.K. Kanjarla, R.A. Lebensohn, L. Balogh, C.N. Tomé, Study of internal lattice strain distributions in stainless steel using a full-field elasto-viscoplastic formulation based on fast fourier transforms, Acta Mater. 60 (2012) 3094–3106, https://doi.org/10.1016/j.actamat.2012.02.014.
[52] M. Morán, M. Vicente Álvarez, P. Vizcaíno, D.W. Brown, J. Santisteban, Dislocation density evolution in cold-rolled Zr-2.5%Nb pressure tubes under thermal

treatments by high energy XRD and neutron TOF diffraction peak profile analysis, J. Alloys Compd. 929 (2022) 167196, https://doi.org/10.1016/j.jallcom.2022.167196.
[53] A. Boulle, C. Legrand, R. Guinebretière, J.P. Mercurio, A. Dauger, X-Ray diffraction line broadening by stacking faults in $SrBi_2Nb_2O_9/SrTiO_3$ epitaxial thin films, Thin Solid Films 391 (2001) 42–46, https://doi.org/10.1016/S0040-6090(01)00975-0.
[54] L. Balogh, G. Ribárik, T. Ungár, Stacking faults and twin boundaries in fcc crystals determined by x-ray diffraction profile analysis, J. Appl. Phys. 100 (2006) 023512, https://doi.org/10.1063/1.2216195.
[55] D.A. Wigley, Mechanical properties of materials at low temperatures, Cryogenics 8 (1968) 3–12, https://doi.org/10.1016/S0011-2275(68)80042-6.
[56] X. Wen, L. Zhu, M. Naeem, H. Huang, S. Jiang, H. Wang, X. Liu, X. Zhang, X.-L. Wang, Y. Wu, Z. Lu, Strong work-hardenable body-centered-cubic high-entropy alloys at cryogenic temperature, Scr. Mater. 231 (2023) 115434, https://doi.org/10.1016/j.scriptamat.2023.115434.
[57] Z. Zhang, F. Shen, H. Liu, M. Könemann, S. Münstermann, Temperature-dependent deformation and fracture properties of low-carbon martensitic steel in different stress states, J. Mater. Res. Technol. 25 (2023) 1931–1943, https://doi.org/10.1016/j.jmrt.2023.06.070.
[58] T. Ungár, I. Dragomir, Á. Révész, A. Borbély, The contrast factors of dislocations in cubic crystals: the dislocation model of strain anisotropy in practice, J. Appl. Crystallogr. 32 (1999) 992–1002, https://doi.org/10.1107/S0021889899009334.
[59] V. Vitek, Core structure of screw dislocations in body-centred cubic metals: relation to symmetry and interatomic bonding, Phil. Mag. 84 (2004) 415–428, https://doi.org/10.1080/14786430310001611644.
[60] U. Essmann, H. Mughrabi, Annihilation of dislocations during tensile and cyclic deformation and limits of dislocation densities, Philos. Mag. A 40 (1979) 731–756, https://doi.org/10.1080/01418617908234871.